Materials & Design 220 (2022) 110901

Contents lists available at ScienceDirect

Materials & Design

journal homepage: www.elsevier.com/locate/matdes

Room temperature and high-temperature properties of extruded Ti-4Fe-3W/2TiC composites in α+β and β phases

Abdollah Bahador [a,*], Ayhan Yurtsever [b], Astuty Amrin [c], Shota Kariya [a], Junko Umeda [a], Jianghua Shen [d], Biao Chen [e], Takeshi Fukuma [b], Katsuyoshi Kondoh [a,*]

[a] JWRI, Osaka University, 11-1 Mihogaoka, Ibaraki, 567-0047 Osaka, Japan
[b] Nano Life Science Institute (WPI-NanoLSI), Kanazawa University, Kanazawa 920-1192, Japan
[c] Razak Faculty of Technology and Informatics Universiti Teknologi Malaysia, 54100 Jalan Sultan Yahya Petra, Kuala Lumpur, Malaysia
[d] School of Aeronautics, Northwestern Polytechnical University, Xi'an 710072, China
[e] State Key Laboratory of Solidification Processing, Northwestern Polytechnical University, Xi'an 710072, China

HIGHLIGHTS

- Novel Ti-4Fe-3W/2TiC composite utilizing spark plasma sintering and hot extrusion.
- Extruded composite at α+β exhibited yield strength of 1215 MPa at room temperature.
- Extruded composite at β showed a consistent strength at high temperatures.
- TiC dispersion was identical, while α morphology of the alloy matrixes was different.

GRAPHICAL ABSTRACT

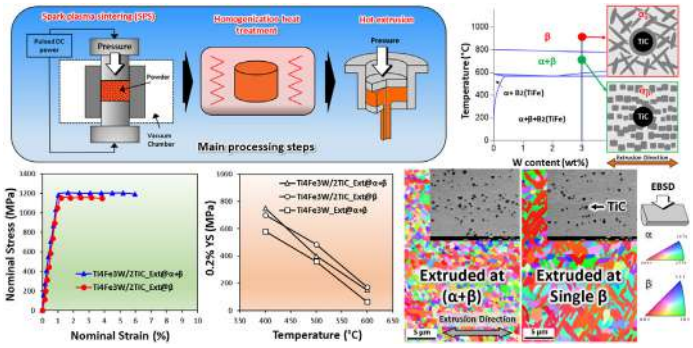

ARTICLE INFO

Article history:
Received 10 April 2022
Revised 21 June 2022
Accepted 24 June 2022
Available online 28 June 2022

Keywords:
Titanium matrix composite (TMC)
Hot extrusion
Tensile strength
Microstructure characterization

ABSTRACT

Considering the high strength of titanium matrix composites (TMCs) at room and elevated temperatures, the aim of this study was to develop novel TMC Ti-4Fe-3W/2TiC (wt%) utilizing powder metallurgy and subsequent extrusion at different temperatures: the two-phase (α+β) and pure β phase regions. The TiC particle dispersion was almost identical in both composites with variation in the size distribution. However, there was a significant difference in the morphology of the α phase in the matrix. The α+β-extruded composite exhibited globular α_p (grain size: 0.7 μm); in contrast, the β-extruded phase showed acicular α_s (grain size: 1.5 μm). Additionally, α-Ti was the predominant phase in contact with TiC particles due to the semi-coherent relationship between these two phases. A remarkably high yield strength (1215 MPa) was achieved at room temperature in the α+β -extruded composite, while the β-extruded composite exhibited consistently improved strength at high temperatures. Morphological characterization using atomic force microscopy (AFM) revealed the β phase was slightly harder than the α phase, probably due to the solid solution of Fe and W that predominant in the β phase.

* Corresponding authors.
E-mail addresses: abdollah@jwri.osaka-u.ac.jp (A. Bahador), kondoh@jwri.osaka-u.ac.jp (K. Kondoh).

https://doi.org/10.1016/j.matdes.2022.110901
0264-1275/

1. Introduction

Reinforced titanium matrix composites (TMCs) have received considerable attention due to their improved properties compared with monolithic titanium. The reinforcements are in the form of discontinuous particles or continuous whiskers. Owing to their outstanding characteristics, such as improved mechanical properties and high-temperature durability, TMCs are promising materials for commercial automotive, aerospace, and advanced military applications [1]. The first commercialization of TMCs in the automotive sector was carried out by the Toyota Motor Corporation in 1998 when titanium-based composite materials (Ti/TiB) were adopted for engine valves in mass-produced cars [2]. In recent decades, TMCs have been significantly developed and evaluated for aerospace applications, such as aircraft engines (owing to high specific strength) and airframes (owing to high specific modulus). High-temperature TMCs based on titanium aluminides, offer potential savings in weight of 50% compared to monolithic nickel-based superalloys while maintaining an equivalent strength and stiffness in jet engine propulsion systems [3].

The method used to fabricate TMCs can introduce different characteristics. While the *in situ* process facilitates the production of the finely sized reinforcements and clean interfaces between the reinforcement and the matrix to exhibit enhanced properties [4], the ex situ fabrication of TMCs produces both superior mechanical properties and high wear resistance with stabilized friction coefficient under dry sliding conditions [35]. According to the literature, research efforts on TMCs have primarily focused on the commercially pure Ti (CP-Ti) and conventional Ti–6Al–4V alloys; however, different Ti alloys have recently been successfully used, and the properties were remarkably improved [4,6]. For instance, in the study by Grützner et al. [7], the hardness, stiffness, and compressive strength of a Ti–5Al–5Mo–5V–3Cr alloy were improved using hybrid reinforcement with TiB and TiC ceramic particles. Zherebtsov et al. [8] have reported the enhanced properties of a Ti–15Mo (β-Ti matrix) reinforced with TiB using spark plasma sintering (SPS) and high-pressure torsion.

TiC and TiB are the most effective reinforcements due to their excellent thermodynamic stability and better chemical compatibility; they also have densities (Ti: 4.51, TiB: 4.57, TiC: 4.93 g/cm^3) and thermal expansion coefficients similar to the titanium matrix (TiB and TiC: 7.2 × 10^{-6}K^{-1}, Ti: 8.2 × 10^{-6}K^{-1}) [9]. While TiB provides creep resistance, TiC has been proven to promote flow stress [10,11]. Furthermore, the TiC-reinforced Ti alloys exhibited excellent combined properties, including superior specific strength as well as high-temperature properties [12]. Generally, the combination of CP-Ti with ceramic particles results in low formability because of the incorporation of high-strength and high-modulus reinforcements with a hexagonal close-packed (hcp) matrix that has less system slip. Therefore, thermomechanical processing (TMP), such as hot forging [13], extrusion [14], and rolling [15], improved the formability [16]. Hot extrusion effectively resulted in the grain refinement of the matrix accompanied by dynamic recrystallization (DRX), which has been confirmed to acquire higher strength and better ductility [17,18]. Huang et al. [19] studied the effect of extrusion ratio on the microstructure and mechanical properties of TiC and TiB reinforced Ti–6Al–4V alloys. It was reported that increasing the extrusion ratio not only promotes the dynamic recrystallization (with smaller grain size) but also causes decreasing the aspect ratio of TiB whiskers. This consequently resulted in the enhancement of tensile strength, elastic modulus, and ductility. In similar studies on TMCs, the effect of extrusion temperature and dies angle were investigated systematically. As extrusion temperature increased, yielding gradually occurred at lower stress. The elongation first increased until extrusion temperature of 1030 °C, but after this temperature elongation decreased due to the formation of coarser and dislocation-free α grains [20]. It was also claimed that the extrusion dies angle range of 45–60° was suitable for optimal hot extrusion [21].

Two-phase (α+β) titanium alloys form a wide range of high-performance alloys used for different applications, that is, biomedical and aerospace industries, due to their high specific strength and excellent corrosion resistance. During the manufacture of conventional two-phase titanium alloys, different TMPs, involving a series of steps, are used to obtain a specific microstructure with the desired mechanical properties. The primary hot working of this type of titanium alloy is usually carried out in the β-phase region to develop a lamellar microstructure (transformed microstructure). Although the lamellar microstructure exhibits good strength and fatigue crack growth resistance, it is characterized by relatively low tensile ductility. In contrast, the equiaxed (globular) microstructure is often more desirable for many service applications due to its better balance of high strength and ductility at room temperature, as well as improved fatigue properties. Therefore, the hot deformation of two-phase titanium alloys is usually conducted through subtransus processing (in the α+β region) to break down the lamellar structure and obtain the desired equiaxed microstructure known as globularization.

Although the process of globularization plays a key role in tailoring the microstructure of two-phase titanium alloys, the dynamic microstructure changes (such as recovery and dynamic globularization) are strongly sensitive to the processing conditions and the initial microstructure [17,22]. In our previous works, we have successfully developed Ti–Fe–W alloys (comprised of two-phase microstructural α+β) and determined that the Ti-4Fe-3W (wt%) composition has an excellent strength–ductility trade-off [23,24]. Therefore, we considered this composition as an alloy matrix and developed a novel Ti-4Fe-3W/2TiC TMC using TiC reinforcement particulates via extrusion in the dual-phase (α+β) and β regions. Additionally, there is limited study on the TMC matrix strengthened with W, as such this research is critical to investigate which provides novel information for the development of high-temperature alloys. We demonstrate a different microstructure in the monolithic alloy matrix depends on the extrusion temperature (850 °C and 1000 °C). The microstructure control via hot extrusion as well as TiC reinforcement resulted in improved tensile properties at room and elevated temperatures.

2. Materials and experimental procedure

2.1. Composite preparation

To synthesize the Ti–4Fe–3W/TiC composite, Ti (45 μm, Tohotech), Fe (3–5 μm, high purity chemicals) and W (2 μm, high purity chemicals) and TiC (20–40 nm, PlasmaCem GmbH) powders were used. The pre-mixed powders were prepared using a conventional ball-milling equipment (UBM-S, MASUDA) with a speed of 100 rpm for 6 h to obtain homogeneous blends. SPS was used to densify blends using a graphite die. The heating rate was 20 °C·min^{-1}, and consolidation was conducted at 1000 °C for 1 h in a vacuum atmosphere at 30 MPa uniaxial pressure. The dimensions of the sintered cylindrical samples were 36 × 30 mm diameter and height, respectively. The sintered composites showed undissolved W; therefore, for homogenization, they were subjected to homogenization heat treatment at 1300 °C for 1 h in a vacuum atmosphere to obtain a uniform Ti-4Fe-3W matrix. As-sintered specimens were subsequently heated in an infrared gold image furnace (SSA-P610CP, ULVAC-RIKO) under argon atmosphere at up to 850 °C (α+β) and 1000 °C (single β) and immediately extruded into 10-mm bars (extrusion ratio: 13). Considering the

temperature drop when the sample was removed from the furnace and the load was applied, the former was deformed in the α+β region (according to previous work [24]), while the latter was deformed in the β region.

2.2. Microstructure characterization

The micrograph of powders consisting of different morphologies are shown in Fig. 1. While Ti has an irregular shape, Fe and W have regular geometric globular and polyhedral shapes, respectively. Microstructure characterization was performed on small samples cut from the hot extruded composites and mounted in carbon resin. Mounted samples were polished using abrasive papers up to 2000 grit size, followed by alumina slurries. A field emission scanning microscope (FESEM, JSM-6500F, JEOL) at an acceleration voltage of 15 V was used for microstructure observation. An electron backscatter diffraction (EBSD) system was used to evaluate the crystallographic orientation and analyze constituent phases. The EBSD samples were prepared using a vibratory polishing machine (VibroMet® 2, Buehler) for 8 h in a silica solution. To collect the data, the sample was scanned at an operating voltage of 15 V and a step size of 50 nm. A high-resolution transmission electron microscope (HRTEM, JEM-2100F, JEOL) operating at 200 kV was employed for a detailed study of the microstructure. The TEM samples were prepared using a focused ion beam (MultiBeam FIB system, JIB-4500) incorporated in a scanning electron microscope (SEM) operated at 30 kV. The oxygen, nitrogen, and hydrogen contents were measured for pre-mixed powders and extruded specimens using an oxygen–nitrogen–hydrogen analyzer (EMGA-830, HORIBA). The average size of TiC particles was measured using imageJ software. The size of approximately 80 to 100 particles was measured in both composites and the average size was obtained.

2.3. Evaluation of mechanical properties

A uniaxial tensile test was performed on samples prepared by wire-cut electrical discharge machining to evaluate the mechanical properties. The samples were 1 × 2 mm in the center with a gauge length of 10 mm. The room temperature tensile test was conducted on three test samples using a universal testing machine (AUTOGRAPH AG-150 KN, Shimadzu) at a strain rate of 5×10^{-4} s^{-1}. The displacement was recorded with an advanced digital CCD camera and a non-contact extensometer system. The samples (two samples for each condition) used to evaluate high-temperature tensile properties were annealed at test temperatures (400 °C, 500 °C, and 600 °C) for 100 h to simulate the high-temperature operation condition, under an argon atmosphere before the test was performed using a horizontal high-temperature tensile testing machine (CATY-T3H, YONEKURA MFG). The microhardness was measured using a Shimadzu (HMV-G) tester to apply a 980.7 mN force for a 10 s dwell time. To verify the accuracy of the results, 25 points in a rectangular pattern were measured for each specimen, and the average value was calculated and used.

2.4. Atomic force microscopy (AFM) characterization

The local structural properties of the prepared composite surfaces were characterized using a Bruker BioScope Resolve AFM system operating in PeakForce Tapping mode with ScanAsyst Air. The AFM images were acquired using RTESPA-525 cantilevers (purchased from Bruker) with a nominal spring constant of 200 N/m and a nominal tip radius of 8 nm. We experimentally determined the individual spring constant of each cantilever using the standard thermal tune method [25]. AFM image rendering and data processing were performed by using the NanoScope Analysis software (version 1.9, Bruker, Billerica, MA, USA).

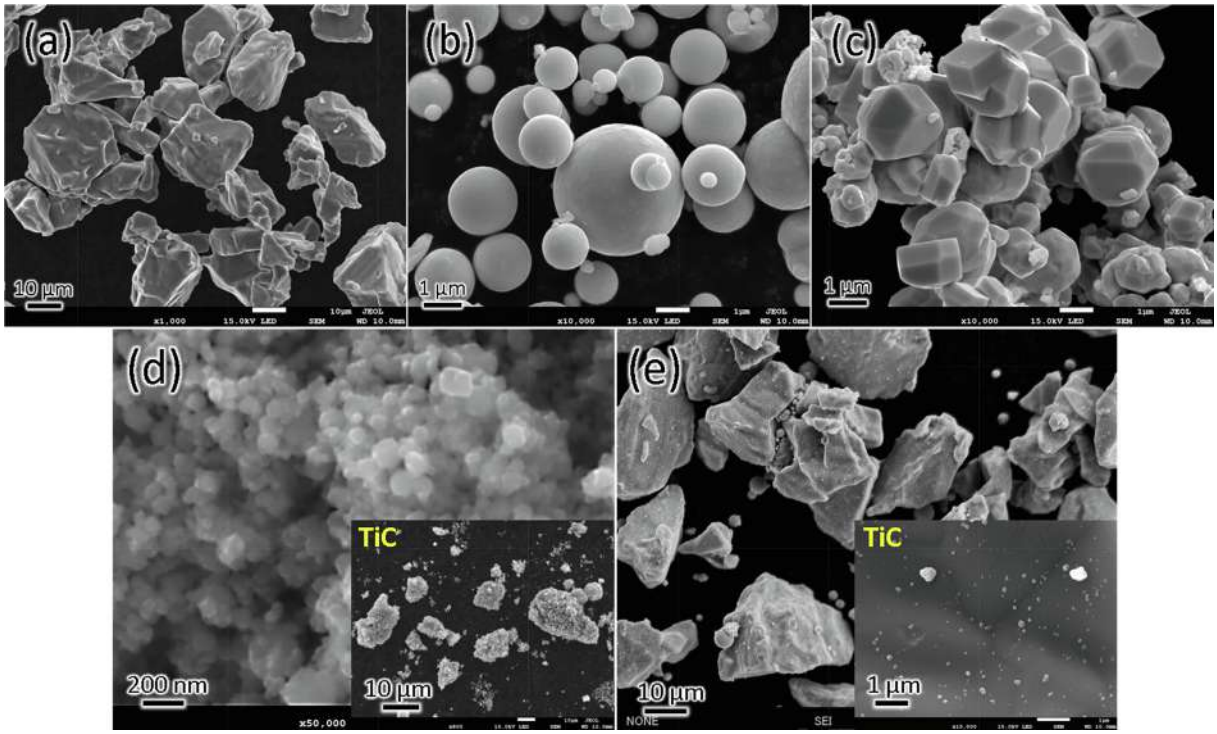

Fig. 1. SEM images showing the morphology of the raw (a) Ti, (b) Fe, (C) W powders, (d) TiC nanoparticles, and (e) pre-mixed powder with TiC nanoparticles distributed on the Ti powder.

3. Experimental results

3.1. Microstructural characterization

Fig. 1 shows the SEM images of the starting materials. The micrographs of the raw powders used to form the matrix exhibited different morphologies. While the Ti powder contained irregular particles, the Fe and W powders consisted of regular globular and polyhedral particles, respectively. The agglomeration of 10–50 μm in the starting TiC nanoparticles was observed. The uniform distribution of TiC on the Ti powder surface after conventional ball milling is shown in Fig. 1(e). The size and morphology of the TiC nanoparticles were also investigated using TEM, as shown in Fig. 2. TEM images revealed grain sizes of 20–130 nm with polyhedron morphology as well as crystallographic information.

The SEM micrographs of the extruded bars are illustrated in Figs. 3 and 4. As seen at low magnification, the dark spots represent the agglomerated TiC particles that provided the micro-sized reinforcements of the alloy matrix. This agglomeration of TiC nanoparticles was inevitable owing to the large specific surface areas and van der Waals forces. However, recently, agglomeration-free nanoscale TiC-reinforced titanium matrix composite has been reported using *in situ* laser additive manufacturing [26]. The TiC particles appeared similarly dispersed in both composites with a maximum agglomerated particle size of about 11 ± 0.5 μm and an average size of 5 ± 0.5 μm; however, the size distribution were different. The size distribution in the α+β-extruded composite was more uniform than in the β-extruded composite where the fraction of smaller particles is higher, particularly those $\leq$ 6 μm.

The alloy matrix comprised two phases, including α and β Ti. A large difference in the α phase morphology was observed. The α+β-extruded composite was comprised of equiaxed/globular primary α_p (transformed from acicular α phase in the sintered alloy); in contrast, acicular secondary α_s formed in the β-extrude composite (transformed from prior β). The phase diagram shown in Fig. 4 was obtained by Pandat software. It exhibits α+β and β phase stability and related transformation temperatures (α+β ↔ β). The effect of extrusion in α+β and β regions on the microstructure, in particular, α phase morphology was illustrated using schematic images. High magnification observations revealed that the TiC particles were in contact with both the α and β phases in the α+β-extruded composite, while α is the predominant phase interfaced with the TiC particles in the β-extruded composite. Furthermore, local microcracks and debonding were observed in the agglomerated regions (yellow arrows in Figs. 3 and 4), which may be attributed to the local friction and shearing of agglomerated hard particles via material flow and severe plastic deformation during extrusion. The plastic deformation around the TiC particles is more prominent in Fig. 3 than Fig. 4 due to the lower extrusion temperature of the α+β region, where the flow pattern was screened by phase transformation taking place after material flow.

The oxygen, nitrogen, and hydrogen content of the pre-mixed powders and extruded composites, as well as the monolithic alloy and powders, are shown in Table 1. This measurement was conducted to quantitatively evaluate the solid solution strengthening effect, especially those of oxygen and nitrogen, which significantly affect the material properties [18,27]. In general, we aim to control the amount of oxygen, nitrogen, and hydrogen by conducting the SPS and pre-heating for extrusion under high vacuum and argon gas, respectively. However, the extruded composites have a slightly higher content of these elements than the monolithic alloy which may be related to their permeability of them from contamination and air exposure during extrusion.

Figs. 5 and 6 show the EBSD analysis of the Ti-4Fe-3W/2TiC composites extruded at α+β and single β, respectively. Fig. 5 includes a general view of the inverse pole figure (IPF), the separated IPF corresponding to the α phase, and pole figure mapping to understand the grain orientations. IPF maps are analyzed by the indices of crystal planes which are identified as red, blue, and green. These colors represent (0001), (10 $\bar{1}$0), and (11$\bar{2}$0) crystal planes, respectively. Fig. 6 additionally presents the prior β phase grains which are reconstructed using OIM-EBSD software to understand the β → α phase transformation. Similar to the SEM observations, the morphology differences of the α grains depended on the extrusion temperature. While extrusion in the α+β region resulted in equiaxed (globular) features, extrusion in the β region led to acicular morphology. The average grain size in the α+β-extruded composite was much smaller (0.7 ± 0.05 μm) compared to the single β-extruded composite (1.5 ± 0.15 μm).

Furthermore, texture analysis showed that α_p in Fig. 5 has higher intensity (I_{max} = 9) than α_s (I_{max} = 4.5) in Fig. 6a for (10 $\bar{1}$ 0) prismatic planes. It is noteworthy to mention that during extrusion of Ti alloys {0001} basal planes are highly oriented in normal to the extrusion direction (ED), which indicates < 10 $\bar{1}$ 0> // ED strong texture formation. Similar texture development has been reported by Umeda et al. for Ti–Fe alloys extruded in the α +β and single β phase regions [28]. Additionally, as shown in Fig. 6b, in some locations, a strong basal texture < 0001 > can be

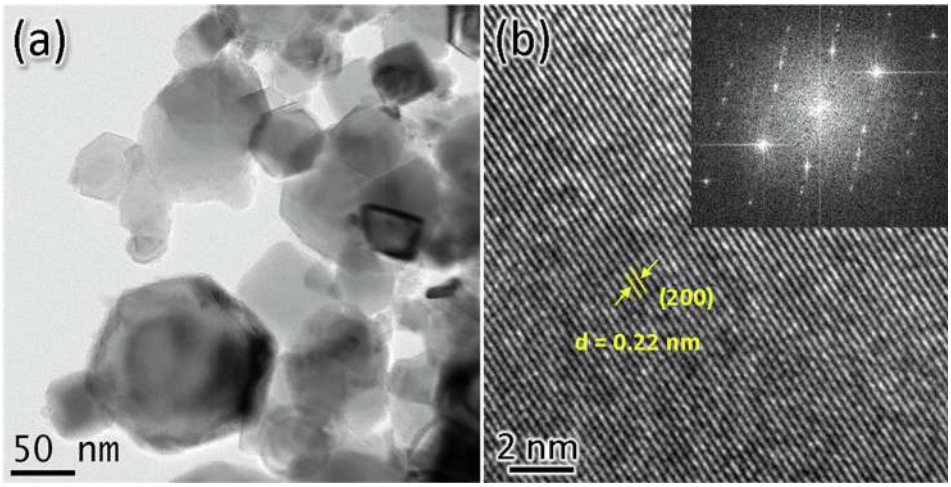

Fig. 2. (a) TEM bright field image and (b) HRTEM observation of the lattice fringes of TiC nanoparticles with crystallographic information.

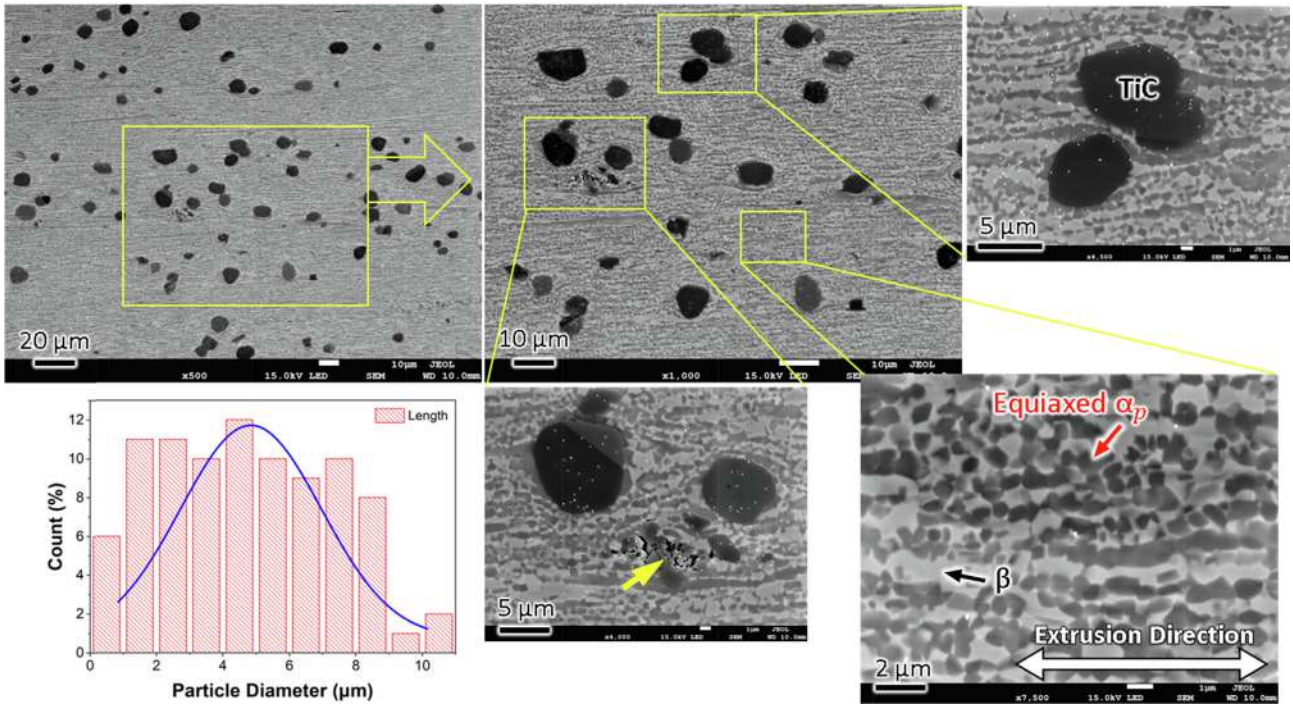

Fig. 3. SEM images of α+β-extruded Ti-4Fe-3W/2TiC composite and TiC particle size distribution.

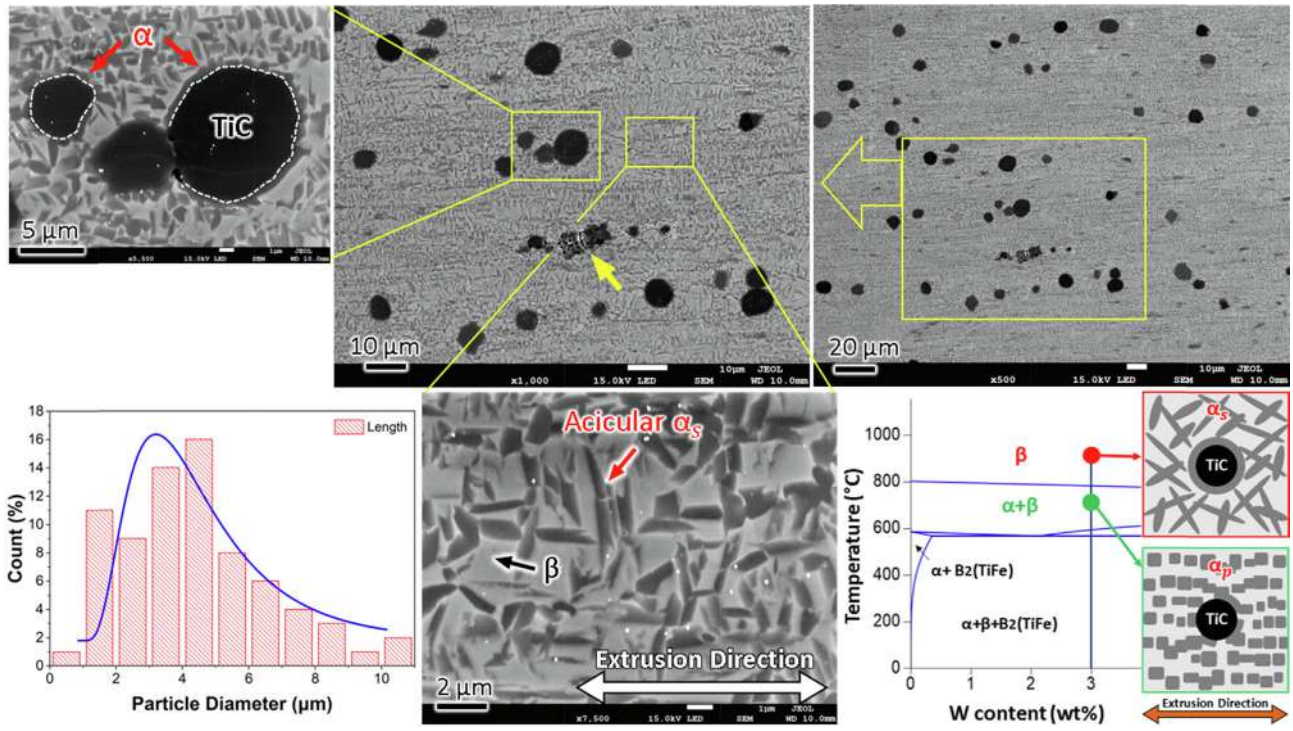

Fig. 4. SEM images of the single β-extruded Ti-4Fe-3W/2TiC composite and the TiC particle size distribution, and schematic illustration of the microstructure evolution due to different extrusion temperatures.

found (I_{max} = 39.8). According to Germain et al.[29], extrusion in the β phase can also result in strong variant selection during the β → α_s phase transformation. However, this work indicated that this strong texture due to variant selection could be influenced by the orientation and grain size of the prior β grains. Smaller grain sizes with different orientations caused different α_s orientations, resulting in lower texture formation (Fig. 6a). In contrast, when there are coarse prior β grains with similar preferential orientation, ⟨1 1 0⟩ β, the phase transformation is very compatible, and as a

Table 1
Oxygen, nitrogen, and hydrogen contents of pre-mixed and extruded composites and the monolithic alloy matrix.

	Oxygen content (wt%)	Nitrogen content (wt%)	Hydrogen content (wt%)
Pre-mixed powders Ti-4Fe-3W	0.24	0.03	0.001
α+β-extruded Ti-4Fe-3W	0.25	0.04	0.003
Pre-mixed powders Ti-4Fe-3W/2TiC	0.32	0.08	0.007
β-extrude Ti-4Fe-3W/2TiC	0.34	0.09	0.007
α+β-extruded Ti-4Fe-3W/2TiC	0.34	0.09	0.008

result, a strong texture with < 0001 > α_s normal to the ED is formed.

3.2. Tensile properties at room temperature

The nominal stress–strain curves of Ti-4Fe-3W/2TiC composites obtained from the room temperature tensile tests are shown in Fig. 7(a). Both composites exhibited excellent yield strength at 0.2% offset (0.2 %YS) of approximately 1215 MPa and 1105 MPa for the extrusion conditions α+β and β, respectively. This strength is higher than that of conventional Ti–6Al–4V [30] and Ti–6Al–4V strengthened with TiC [6] or W particles [31]. The extruded composite in the α+β not only showed higher strength than the composite extruded in the single β phase but it also showed a higher elongation (6.5%) in comparison with that of the composite extruded at α+β (4%). This tensile behavior can be attributed to the difference in grain size and microstructure morphologies. It is well accepted that grain refinement and globular microstructure enhance the room temperature strength in two-phase Ti alloys [18]. The tensile behavior of the monolithic Ti-4Fe-3W alloy is illustrated in Fig. 7(b) as a reference material with a yield strength of approximately 1123 MPa and elongation to break of 26%. The mechanical properties are summarized in Table 2. A decrease in the elongation at break of the composites compared to the reference alloy was observed.

Fig. 8 presents the fractography and EDS analysis of the extruded compositesof the extruded composites following failure during the tensile test. The matrix of the composites showed a dimpled surface structure, which indicates the ductile fracture mode of the matrices. In metal matrix composites, the load is effectively transferred to the stronger reinforcement particles under the condition where the proper interfacial bonding is achieved. In this case, two failure modes are possible; particle fracture or particle pull-out [32]. The SEM fractography revealed that the fracture of the TiC reinforcement particles is the dominant failure mode. The fractured TiC particles exhibited cleavage, flat-fractured surfaces, and microcracks (yellow arrows, Fig. 8); however, particle pull-out was observed in a few locations (red arrows, Fig. 8). These microcracks could form from two main mechanisms; the first is the brittle nature of the TiC particles along with strong bonds to the alloy matrix. The second mechanism could be related to the agglomeration of the nanoparticles with incomplete bonding, which acts as a source of the microcracks during deformation (as seen in the microstructure of the extruded composites in Figs. 3 and 4). This suggests that cracks initiated at the TiC particles and propagated through the matrix. Due to the small distance between the particles, these microcracks merged in a short time. As a result, early fractures with limited elongation occurred. This phenomenon shows the negative effect of the agglomeration of TiC nanoparticles on the elongation of the fabricated composites. Furthermore, the lack of debonding between the particle and the matrix implies a strong interfacial bonding.

3.3. Tensile properties at elevated temperatures

To evaluate the tensile properties at high temperatures, fabricated composites were loaded uniaxially at different temperatures until fracturing occurred. Fig. 9(a) illustrates the stress–strain curves of materials tested at 400, 500, and 600 °C. The flow stresses were greatly influenced by the deformation temperature: as the test temperature increased, yielding occurred at lower stress levels. Flow stress rapidly reached a peak due to the accumulation of dislocations, followed by a monotonic decrease until fracturing occurred. The deformation at high temperature triggered dislocation glide and annihilation, resulting in decreased dislocation multiplication and density. Furthermore, the accumulated dislocation energy upon the yielding of materials could provide a sufficient driving force for flow softening via dynamic recovery and recrystallization [33]. During the testing at 400 °C, the composite extruded in the α+β region exhibited slightly higher yield strength

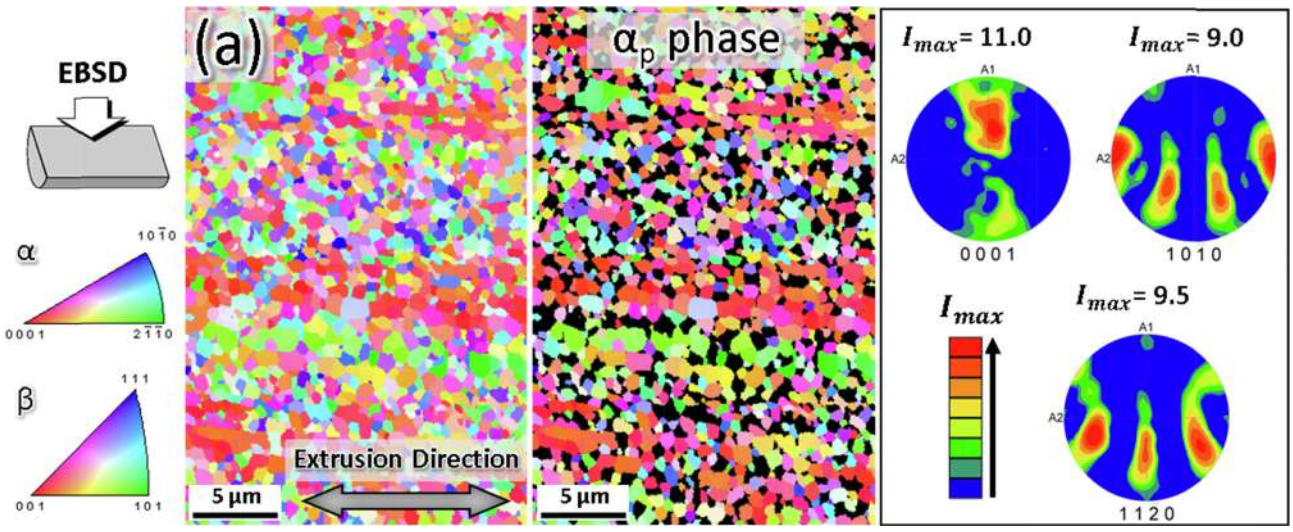

Fig. 5. EBSD analysis of the Ti-4Fe-3W/2TiC composite extruded in the α+β phase.

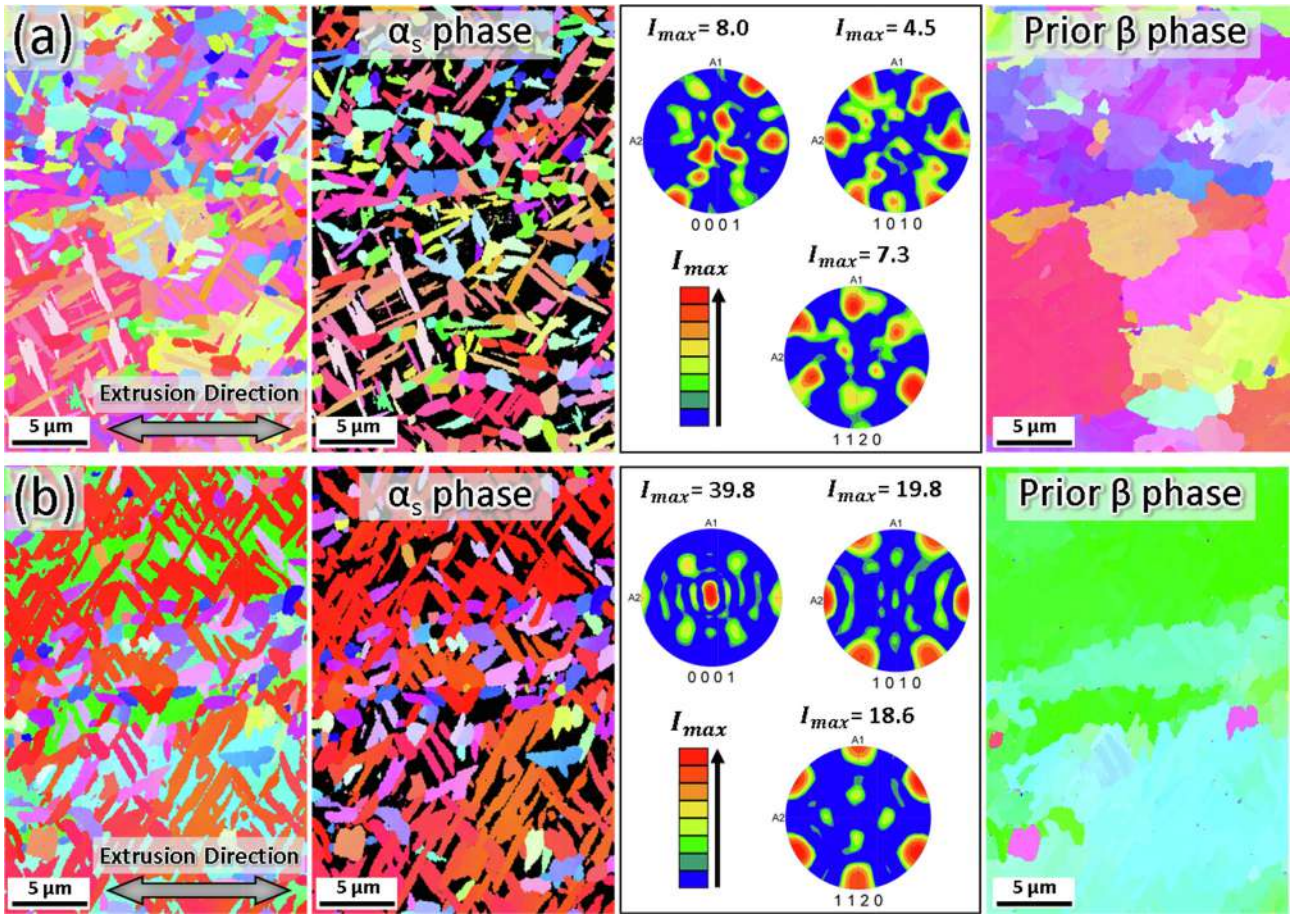

Fig. 6. EBSD analysis of the Ti-4Fe-3W/2TiC composite extruded in the β phase showing (a) low texture and (b) high texture of transformed α, depending on the prior β phase grain size and orientation.

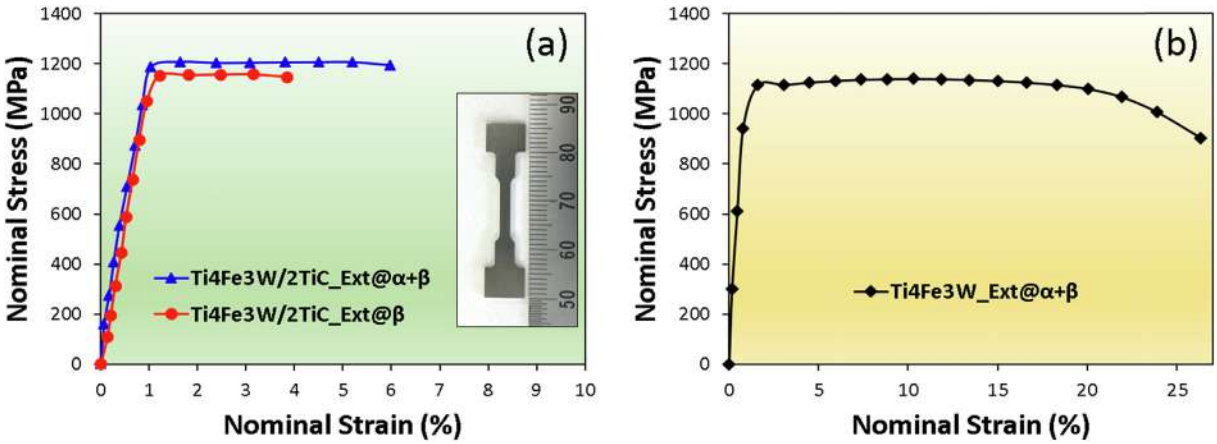

Fig. 7. (a) Nominal stress–strain curves of the Ti-4Fe-3W/2TiC composites and (b) alloy matrix Ti-4Fe-3W tested at room temperature.

Table 2
Room temperature mechanical properties of extruded composites and alloy matrix.

Material	Extrusion region	0.2% YS (MPa)	Elastic modulus (GPa)	Elongation (%)	Microhardness (Hv)
Ti-4Fe-3W/2TiC	α+β	1215	121.7	6.5	412
Ti-4Fe-3W/2TiC	β	1135	120	4	416
Ti-4Fe-3W	α+β	1123	126	26	374

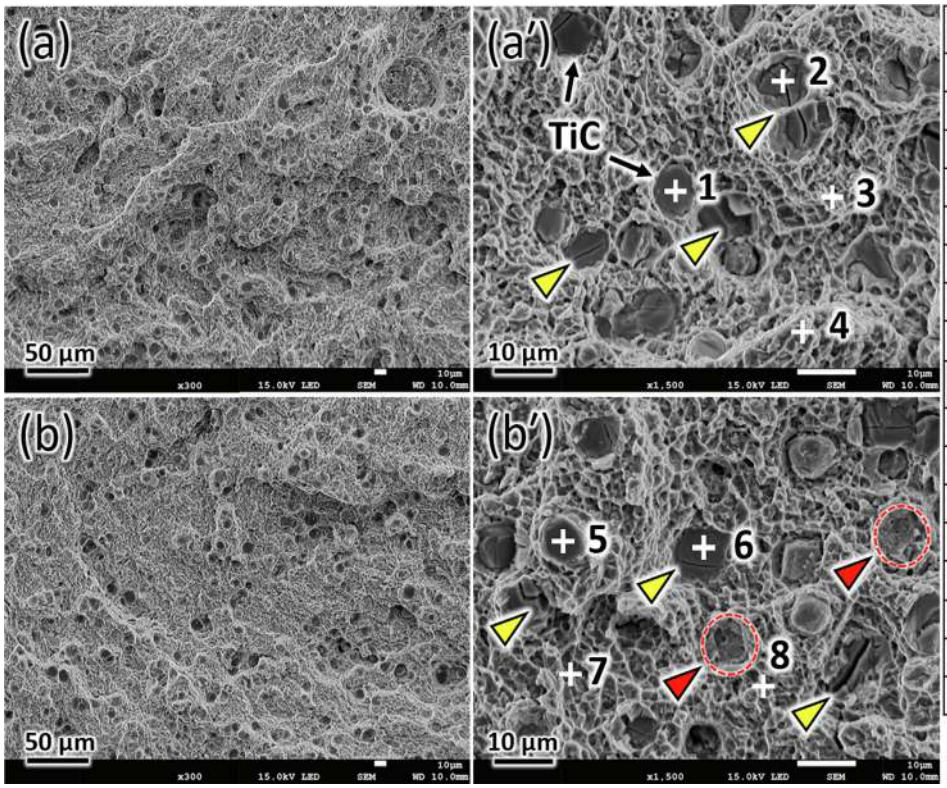

wt%	Ti	Fe	W	C
1	93.89	0.05	0.12	5.93
2	93.81	0.05	0.32	5.82
3	91.30	5.18	3.52	-
4	90.38	6.41	3.21	-
5	93.75	-	0.23	6.03
6	93.77	0.05	0.25	5.92
7	93.44	3.58	2.99	-
8	90.26	5.63	4.11	-
at%	Ti	Fe	W	C
5	79.82	0.04	0.03	20.11
6	80.08	0.03	0.07	19.82
7	94.45	4.60	0.95	-
8	93.45	5.68	0.87	-
5	79.56	-	0.05	20.39
6	79.80	0.04	0.06	20.11
7	96.05	3.15	0.8	-
8	93.87	5.02	1.11	-

Fig. 8. Fracture surface analysis of Ti-4Fe-3W/2TiC composites extruded at (a, a′) α+β and (b, b′) β, including EDS analysis.

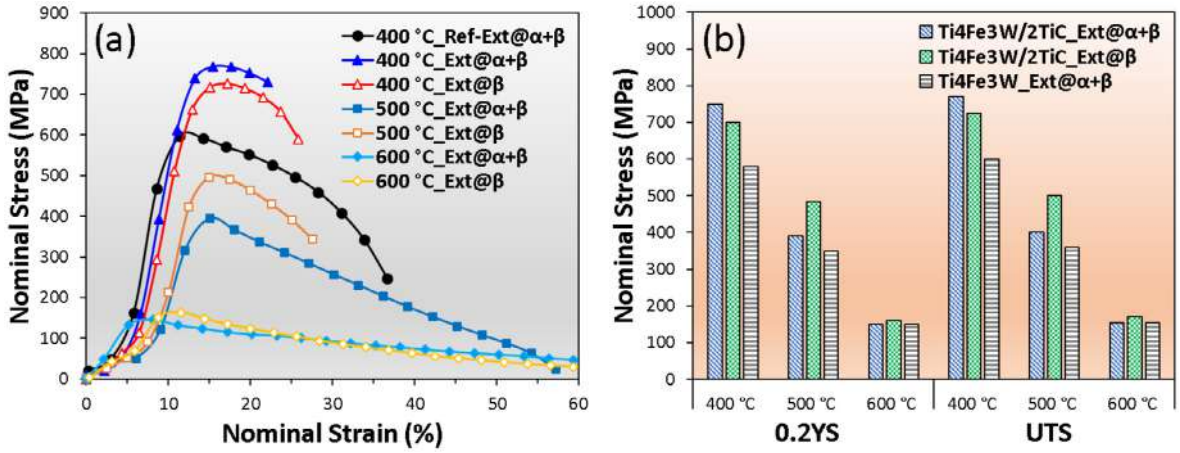

Fig. 9. (a) Tensile behavior of Ti-4Fe-3W/2TiC composites at 400, 500, and 600 °C (b) summary of test results at elevated temperatures compared with the Ti-4Fe-3W alloy matrix.

(~750 MPa) than the composite extruded in the β region (~700 MPa), which could be related to the finer globular microstructure.

In contrast, there was a considerable difference in the yielding points of these composites at 500 °C, where the β-extruded composite showed higher yielding strength (~500 MPa) than the composite extruded in the α+β region (~400 MPa). The acicular α phase resists more effectively at elevated temperatures than equiaxed grains. When the test temperature was increased to 600 °C, both composites showed the lowest strength, approximately ~150 MPa, which is related to the softening of materials at high temperatures. Fig. 9(b) shows the dependence of the high-temperature tensile strength of the monolithic Ti-4Fe-3W alloy and its composites containing 2 wt% TiC. The strength of the TiC-reinforced composites improved at elevated temperatures (specially at 400 and 500 °C). Thus, the composite extruded in the β region showed a consistent strength higher than the monolithic alloy during tensile loading at elevated temperatures.

To elucidate the high-temperature properties of fabricated composites, microstructure observations were conducted with EBSD. Fig. 10 presents the IPF map of the extruded composites after annealing at 400, 500, and 600 °C for 100 h. The α+β-extruded composite exhibited a consistent microstructure at elevated temperatures with similar microstructures appearing after annealing at 400 and 500 °C with an identical average grain size of 1.3 ± 0.15 µm. Annealing at 600 °C resulted in a slight change in the microstructure and grain growth (average grain size of 1.7 ±

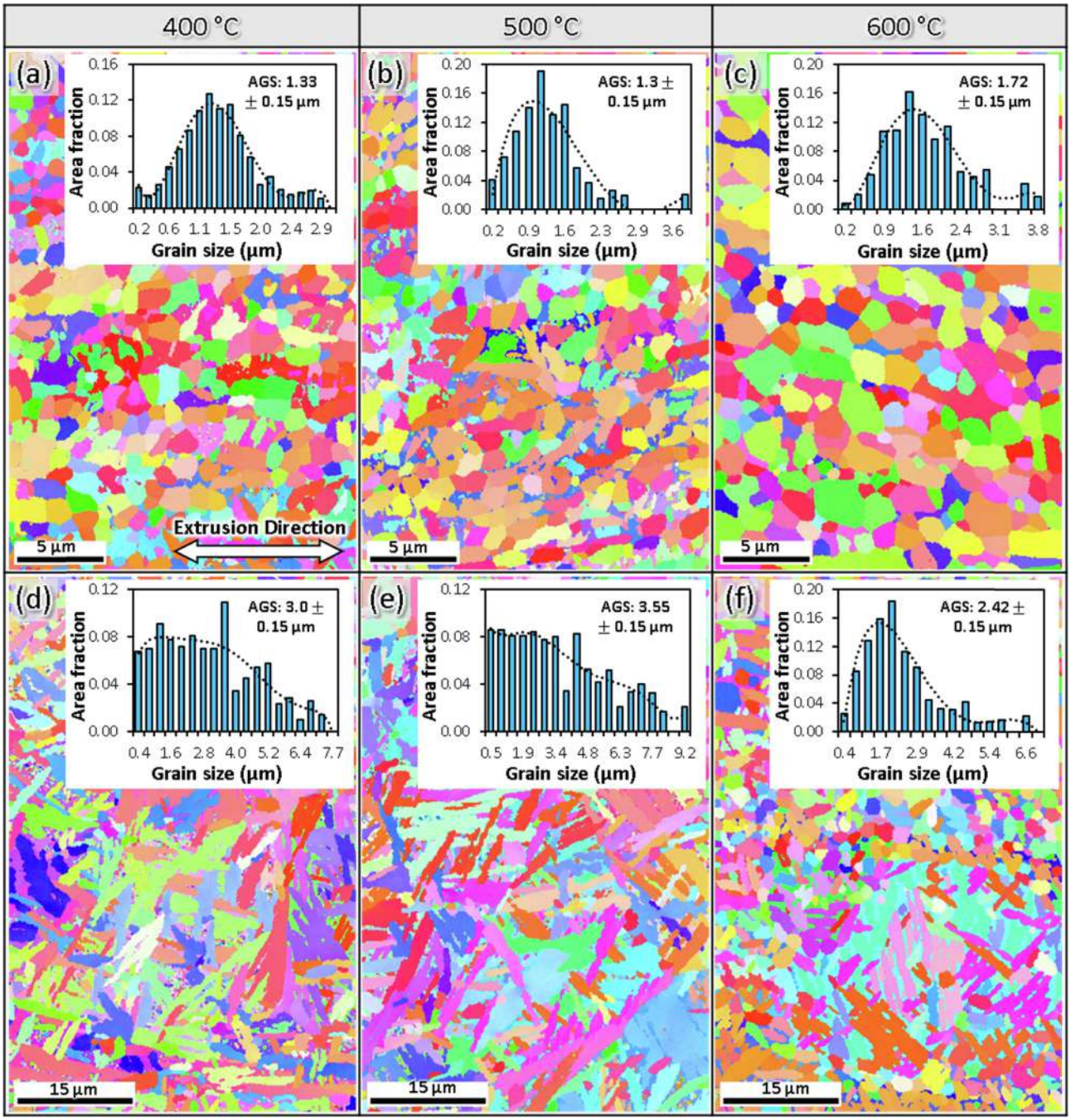

Fig. 10. EBSD evaluation of microstructural stability of Ti-4Fe-3W/2TiC composites at 400, 500, and 600 °C, which have been extruded in the (a-c) α+β and (d-f) β regions (AGS: average grain size).

0.15 μm). In contrast, the annealing of a single β-extruded composite showed a microstructural change with α-colony formation. The microstructure at 500 °C included coarser α colonies after annealing compared with the microstructure at 400 °C. The average grain size was approximately 3 μm and 3.55 ± 0.15 μm for 400 and 500 °C, respectively. Annealing of this material at 600 °C exhibited bimodal microstructure development consisting of α colonies and equiaxed morphology. The grain size was smaller than that at lower annealing temperatures with an average grain size of 2.42 ± 0.15 μm. This behavior may be related to recovery and recrystallization during annealing at 600 °C. All in all, these observations revealed the microstructure stability of fabricated composites at high temperatures. This can be related to some TiC particles which are located in the grain boundaries. These particles can act as obstacles to grain boundary movement and consequently impede grain growth. As shown in Fig. 11, the EBSD analysis of α+β-extruded Ti-4Fe-3W/2TiC composite after annealing at 600 °C exhibits the TiC particles on the grain boundaries using IPF and corresponding image quality (IQ) map constructed from electron backscatter diffraction.

3.4. Characterization of composites using AFM

AFM was used to characterize the local structural properties of the prepared TMC surfaces. AFM has previously been used to investigate the nanoscale surface morphology, slip bands formation, and

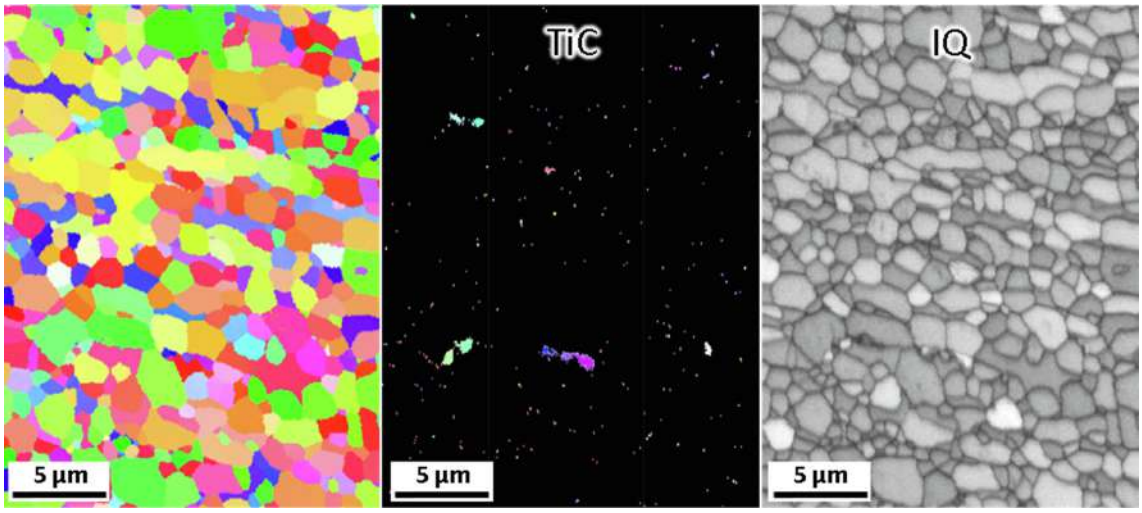

Fig. 11. TiC particles observation on the grain boundaries of α+β-extruded Ti-4Fe-3W/2TiC composite after annealing at 600 °C (using EBSD analysis: IPF and IQ image) which can impede the grain growth at high-temperatures.

strain fields measurement in two-phase materials [34,35]. Fig. 12 shows a typical surface morphology, as well as a 3D image and surface roughness profile obtained from Ti-4Fe-3W/2TiC composites extruded in the α+β and β regions using AFM perpendicular to the ED. The main constituents, including TiC particles, α, and β phases, are resolved in the AFM surface topography images. Representative line profiles taken from the different locations on the surface are presented in Fig. 12(a,b). The β phase exhibited slightly higher topographic height, approximately 4.5 nm higher than the α phase in both composites, except for some areas in the α+β-extruded composite, where the difference was considerably higher, about 10 nm (L_2). However, the marginal difference between the β and α phases has been attributed to the diffusion of Fe and W in the β phase [24], which results in a slight increase in the hardness that affects the surface roughness during mechanical polishing. While TiC showed similar topographic height variation as α_s in the single β-extruded composite, it had higher amplitude than α_p in the α+β-extruded composite.

Additionally, Fig. 12a reveals that the α_r phase formed around the TiC particles, as resulted from the reaction between the reinforcement particle and the matrix, has a slightly lower amplitude than α_s, suggesting that the new α_r has a lower solution element content. Compared to a previous AFM study on the Ti–6Al–4V/TiC [36] composite, the materials in this study showed the TiC profile of lower amplitude. We used the *ex situ* method in our study, while TiC has previously been introduced to Ti–6Al–4V by the *in situ* process where it was formed from the chemical reaction of the initial elements [36]. Therefore, there is a possibility of a higher carbon content and increased hardness and amplitude.

4. Discussion

4.1. Interface characteristics

The interface characteristic is an important factor in TMCs that significantly affects the mechanical properties. Similar to the Ti–6Al–4V/TiC interface, there are several essential concerns regarding Ti-4Fe-3W/TiC interface. The first concern is the potential chemical affinity between the Ti in Ti-4Fe-3W and the TiC reinforcement particles. This affinity may produce a reaction zone with secondary phases, reducing the interfacial strength [37]. At higher temperatures and longer sintering times, this reaction can lead to the formation of the stable phase Ti_2C in the interfacial boundary between TiC and Ti–6Al–4V, as has been reported by Wanjara et al. [38]. The second concern is the heterogeneous nature of the Ti-4Fe-3W/TiC interface. As shown in the microstructure observations, Ti-4Fe-3W is a duplex Ti matrix that includes the α and β phases, which have different crystallographic structures (hcp and bcc, respectively). That is, two different types of interfaces are present: α-Ti/TiC and β-Ti/TiC interfaces with different strengths are formed between TiC and Ti-4Fe-3W matrix. As a result, the different interfaces influence the interfacial behavior under tensile and compressive debonding [37]. In the case of the Ti–6Al–4V/TiC interface, the main failure mechanism was shear failure associated with interfacial debonding during the compression test [39] and brittle fracture of the TiC particles during the tensile test with good interface bonding behavior [40].

Chemical composition analysis near the interfacial boundary of the TiC particles and the Ti-4Fe-3W matrix using TEM–EDS was used to investigate the C and Ti content in the regions near the interface of the α+β-extruded composite. Due to their ability to stabilize β, Fe and W preferentially diffuse into the β phase (Fig. 13). The linear elemental scanning revealed a narrow region where the C content gradually decreased from the TiC particle toward the α-Ti (Fig. 13). This observation suggests that carbon diffused from the TiC into the titanium alloy matrix. Since C is an α phase stabilizer, this diffusion results in α-phase formation around the TiC reinforcement particle. This was more evident in the β-extruded composite because the temperature was higher, and it promoted the diffusion of the C atoms into the adjoining region in the matrix. However, there was no clear secondary phase formation at the Ti–4Fe–3W/TiC interface due to extrusion at 1000 °C and lower temperatures with lower exposure times. The mechanical property measurements by AFM analysis showed a marginal difference in the strength of the α and β phases in Ti-4Fe-3W. Therefore, there are fewer concerns about the above-mentioned issues regarding the interface in the Ti-4Fe-3W/TiC composites.

The bonding interface between the Ti-4Fe-3W matrix and the TiC particles governed the mechanical properties. As shown in Fig. 13, the interface between the α-Ti and the TiC is clean and smooth, contributing to the load transfer. The α-Ti/TiC interface was further studied using the HRTEM, as shown in Fig. 14. The images of lattice fringes in α-Ti and TiC were converted to inverse fast Fourier transform (FFT) images. The generation of edge dislocations in the matrix near the TiC particles was evident in the

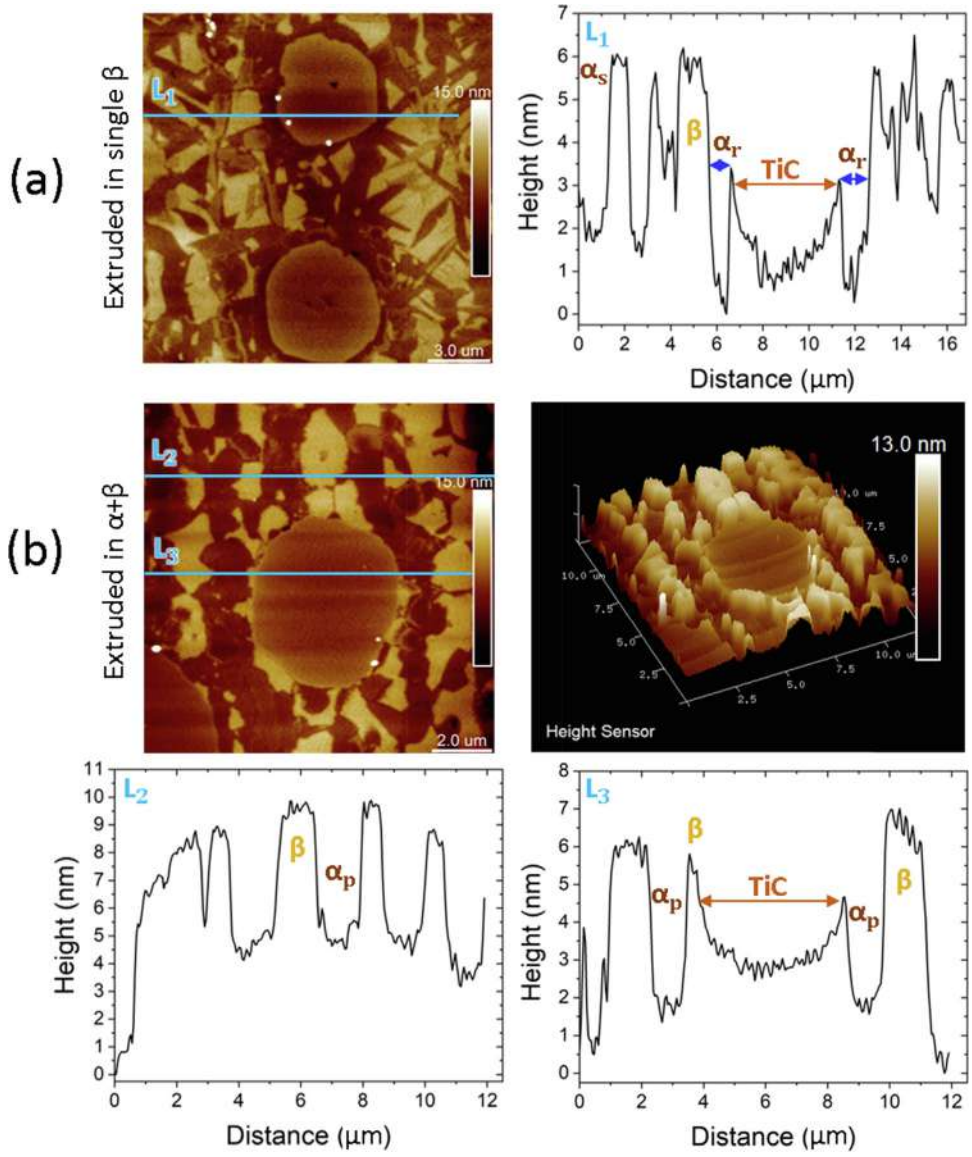

Fig. 12. Typical surface morphology of the composite nanostructures studied by AFM and the representative line profiles taken along the blue lines (L1, L2, and L3) overlaid on the AFM images. (For interpretation of the references to colour in this figure legend, the reader is referred to the web version of this article.)

inverseFFT images, while no dislocations were observed in the reinforcement particles. The formation of dislocations in TMCs is inevitable, and the density of dislocations may depend on the processing methods and parameters. For instance, a dislocation network was reported by Konitzer and Loretto [41] in heat-treated TiC-reinforced Ti–6Al–4V. In addition, the α-Ti and TiC have an $(10\ \bar{1}\ 0)$ α-Ti // (111) TiC orientation relationship where the interplanar crystal spacing of $(10\ \bar{1}\ 0)$ α-Ti and (111) TiC are ~ 0.26 nm and ~ 0.25 nm, respectively. Furthermore, the orientation angle between these two atomic planes was approximately 9°, and it suggested a semi-coherent interface formed between these two phases. This was also supported by a small lattice mismatch between the two phases, which is determined as 1.74% using the following equation [42,43]:

$$F = 2[(nd_{\alpha-Ti} - md_{TiC})/(md_{\alpha-Ti} - nd_{TiC})] \quad (1)$$

where $d_{\alpha-Ti}$ and d_{TiC} are the d-spacings of α-Ti and TiC, respectively, and m and n can be determined by $d_{\alpha-Ti}/d_{TiC} = m/n$ (m and n are integers).

This marginal lattice misfit between α-Ti and TiC promoted the favorable nucleation of α-Ti on the close-packed plane {1 1 1} of TiC. The interface relationship in Ti-4Fe-3W/TiC is in good agreement with the Ti–6Al–4V/TiC interface characterized in a previous study by Ma et al. [44].

4.2. Quantitative analysis of strengthening at room temperature

The strengthening of TMCs reinforced with a particle dispersion is attributed to the synergistic effect of the main factors: load transfer mechanism and dislocation motion-related mechanisms. The load transfer mechanism is based on the inherent properties and the volume fraction of particles, assuming strong interfacial bonding. Dislocation motion-related mechanisms arise from solid solution strengthening, grain refinement, dislocation density, Orowan looping, and the mismatch between properties of the reinforcement particles and the matrix, such as the coefficient of thermal expansion (CTE) [45,24]. The effect of Orowan looping and CTE mismatch were ignored in this study due to the scale of the particle agglomeration (micron-

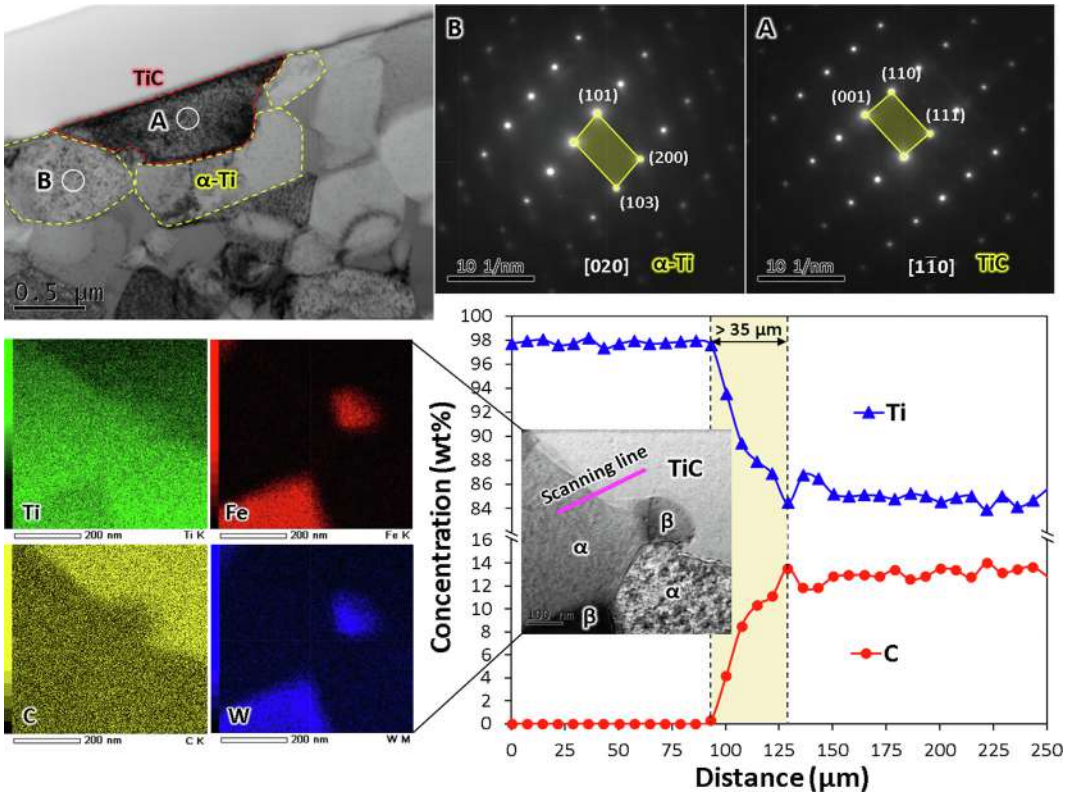

Fig. 13. Chemical composition analysis near the interfacial boundary of TiC particles and the Ti-4Fe-3W matrix (extruded in the α+β region) using EDS/TEM.

sized) and the small difference between the CTEs of TiC and Ti [9]. Thus, the theoretical yield strength of Ti-4Fe-3W/2TiC com-

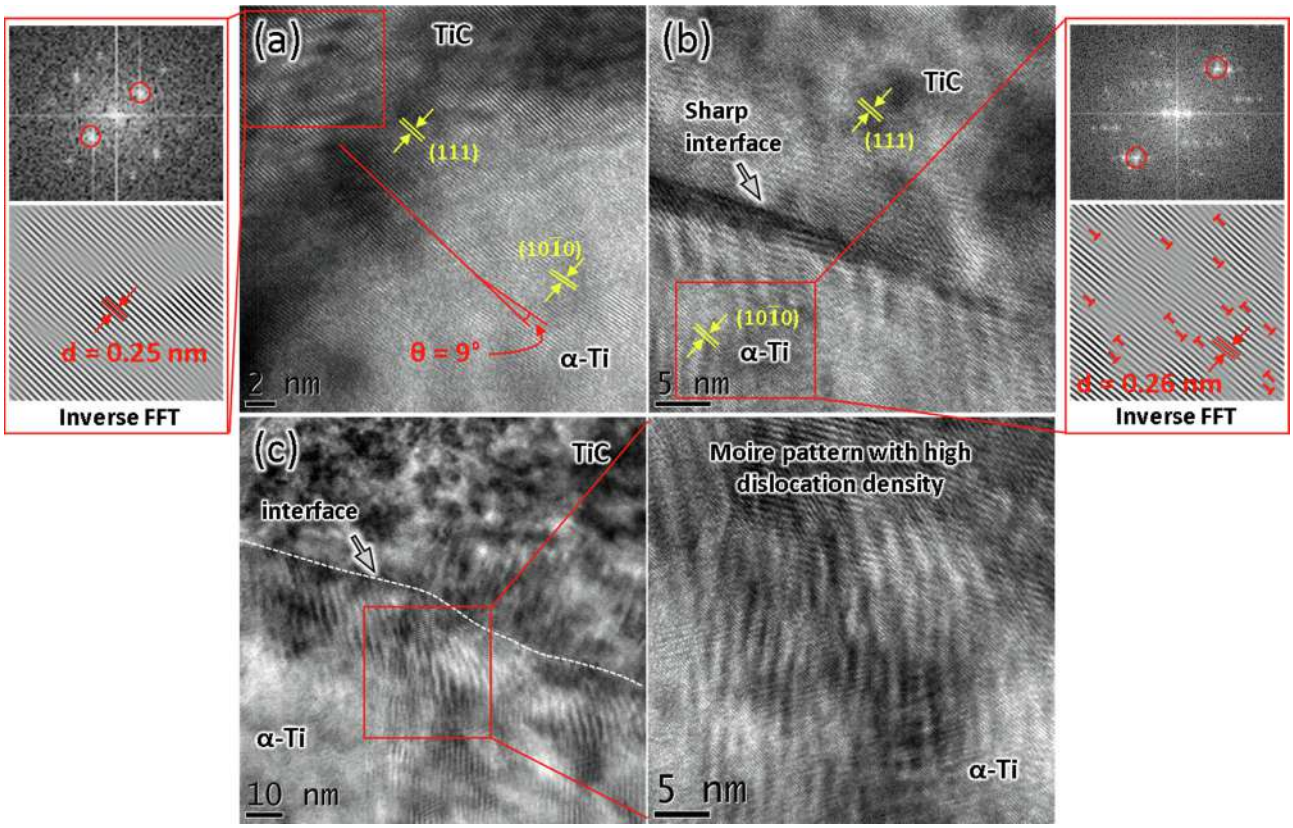

Fig. 14. HRTEM observation of the interface between the Ti-4Fe-3W matrix and TiC particles extruded in the β region.

Table 3
Grain size effect on 0.2% YS of each composite.

Material	Extrusion region	d_m(μm)	d_c(μm)	$\Delta\sigma_{GR}$ (MPa)
Ti-4Fe-3W/2TiC	α+β	9.32 ± 0.46 [24]	0.7 ± 0.05	346 ± 13
Ti–4Fe–3 W/2TiC	β	13 ± 0.9 [23]	1.5 ± 0.15	215 ± 8

posites could be estimated quantitatively using the following equation.

$$\sigma_{TMCs} = \sigma_{Ti} + \Delta\sigma_{LT} + \Delta\sigma_{GR} + \Delta\sigma_{ss} + \Delta\sigma_{Dis} \quad (2)$$

where σ_{TMCs} andσ_{Ti} = 517 MPa [24] are the yield strength of TMCs and pure titanium, respectively.$\Delta\sigma_{LT}$, $\Delta\sigma_{GR}$, $\Delta\sigma_{ss}$ and $\Delta\sigma_{Dis}$ indicate the strengthening caused by load transfer, grain refinement, solid solution (Fe, W, O, N), and dislocation density, respectively. All strengthening factors were similar in both composites except the grain size effect.

4.2.1. Load transfer strengthening

The interface between the TiC particles and the matrix can act as a load transfer medium between the matrix and the particles. Consequently, interface characteristics have an important role in the overall tensile properties. The HRTEM analysis revealed the clean and flowless interface between TiC and α-Ti. The load transfer mechanism was calculated with the following equation [46]:

$$\Delta\sigma_{LT} = 0.5\sigma_{ym}V_f \quad (3)$$

where σ_{ym} is the yield strength of the matrix. Therefore, the strengthening due to load transfer was approximately 10 MPa.

4.2.2. Grain refinement strengthening

The effect of grain size on strengthening was estimated using the Hall–Petch equation as follows [47,18]:

$$\Delta\sigma_{GR} = K\left(d_c^{-0.5} - d_m^{-0.5}\right) \quad (4)$$

where K is a constant of the order of 0.4 MPa $\sqrt{m}$ [48] for Ti, and d_c and d_m are the average grain sizes of the composite Ti-4Fe-3W/2TiC and the monolithic Ti-4Fe-3W alloy matrix, respectively. As shown in Table 3, the increment in the 0.2% YS due to grain refinement is dominant in the α+β-extruded composite.

4.2.3. Solid solution strengthening

To evaluate the solid solution strengthening, we consider O, N, Fe, and W and ignore the effect of hydrogen due to its negligible presence in the materials. Under this assumption, the solid solution strengthening can be written as $\Delta\sigma_{ss} = \Delta\sigma_{O,N} + \Delta\sigma_{Fe,W}$. The strengthening attributed to O and N ($\Delta\sigma_{O,N}$) was estimated as 54 MPa using the Fleischer equation [49,47] ($\Delta\sigma_O = MGb\varepsilon_i^{3/2}X_i^{1/2}$ and $\Delta\sigma_N = MGb\varepsilon_i^{3/2}X_i^{2/3}$) where$M$ = 2.5 is the Taylor factor, G=45 GPa is the shear modulus, and$b$ = 0.296 nm is Burger vector of titanium [47]. The ε_i is an interaction parameter relating to the size and modulus misfits (for oxygen ε_i is 1.112, and for nitrogen, it is 1.002), and X_i is the atomic concentration of the solute atoms (X_O = 1.03 andX_N = 0.31). The solid solution strengthening of Fe and W ($\Delta\sigma_{Fe,W}$ = 240 MPa), as well as the dislocation strengthening ($\Delta\sigma_{Dis}$ = 101 MPa), were similar to the monolithic alloy matrix according to previous work [24]. Therefore, the total calculated yield stress values of Ti-4Fe-3W/2TiC composites extruded at α+β and β are 1268 MPa and 1137 MPa, respectively. These values match well with experimental results.

5. Conclusions

The elemental powders of Ti, Fe, and W were combined with TiC nanoparticles to prepare Ti–4Fe–3 W/2TiC (wt%) composites using SPS. The sintered materials were subsequently extruded in the α+β and β regions. The microstructure characteristics and mechanical properties were evaluated using advanced techniques at room and elevated temperatures. Some interesting conclusions were drawn as follows:

(1) The extruded Ti-4Fe-3W/2TiC composites were composed of a duplex α+β Ti matrix with a similar TiC dispersion, including the agglomeration of particles with a maximum size of approximately 11 ± 0.5 μm and an average size of 5 ± 0. 5 μm.
(2) The distinguished morphology of the α phase in the developed alloy matrix depends on the extrusion temperature. Material extruded in the α+β region exhibited globular/equiaxed shape α_p (grain size: 0.7 μm), while extrusion in the single β phase resulted in acicular α_s (grain size: 1.5 μm).
(3) While TiC particles have an interface with both α-Ti and β-Ti in the composite extruded in the α+β region, α-Ti is the major phase in contact with TiC particles in the composite extruded in a single β phase due to the semi-coherent relationship between these two phases. The clean interface with a good bonding characteristic exhibited an effective load transfer mechanism.
(4) At room temperature, the composite extruded at α+β exhibited a remarkably high yield strength (1215 MPa). In contrast, a consistent strength at high temperature was achieved in the composite extruded at a single β compared to the Ti-4Fe-3W alloy matrix. It showed excellent strengths of 700 and 500 MPa at 400 and 500 °C, respectively.
(5) The evaluation of fabricated TMCs with AFM revealed that the β phase has a slightly higher hardness than the α phase, probably due to the solid solution of Fe and W, which predominated in the β phase.

Data availability

The authors do not have permission to share data.

Declaration of Competing Interest

The authors declare that they have no known competing financial interests or personal relationships that could have appeared to influence the work reported in this paper.

Acknowledgments

This study was financially supported by the Cross-ministerial Strategic Innovation Promotion Program (SIP), "Materials Integration for revolutionary design system of structural materials" (Funding agency: JST), International Joint Research Promotion Program promoted by Osaka University, and the "Project to Create Research and Educational Hubs for Innovative Manufacturing in Asia," Osaka University of the Special Budget Project of the Ministry of Education, Culture, Sports, Science, and Technology-Japan.

The part of this study was financially supported by The Light Metal Educational Foundation. The authors would like to especially thank Mr. Takeshi Murakami for his technical support during TEM observations.

Data availability

The raw/processed data required to reproduce these findings cannot be shared at this time as the data also forms part of an ongoing study.

References

[1] S.C. Tjong, Y.-W. Mai, Processing-structure-property aspects of particulate- and whisker-reinforced titanium matrix composites, Compos. Sci. Technol. 68 (3-4) (2008) 583–601, https://doi.org/10.1016/j.compscitech.2007.07.016.
[2] T. Saito, Affordable high-performance Ti/TiB metal matrix composites tailored for automobile engine components: materials design, manufacturing process, and remaining, Issues 51 (2020) 1–30.
[3] M.D. Hayat, H. Singh, Z. He, P. Cao, Titanium metal matrix composites: an overview, Compos. Part A Appl. Sci. Manuf. 121 (2019) 418–438, https://doi.org/10.1016/j.compositesa.2019.04.005.
[4] S. Li, K. Kondoh, H. Imai, B. Chen, L. Jia, J. Umeda, Microstructure and mechanical properties of P/M titanium matrix composites reinforced by in-situ synthesized TiC-TiB, Mater. Sci. Eng. A. 628 (2015) 75–83, https://doi.org/10.1016/j.msea.2015.01.033.
[5] K. Kondoh, 16 - Titanium metal matrix composites by powder metallurgy (PM) routes, in: M. Qian, F.H. (Sam) Froes (Eds.), Titan. Powder Metall., Butterworth-Heinemann, Boston, 2015: pp. 277–297. https://doi.org/10.1016/B978-0-12-800054-0.00016-2.
[6] H.A. Rastegari, S. Asgari, S.M. Abbasi, Producing Ti-6Al-4V/TiC composite with good ductility by vacuum induction melting furnace and hot rolling process, Mater. Des. 32 (10) (2011) 5010–5014, https://doi.org/10.1016/j.matdes.2011.06.009.
[7] S. Grutzner, L. Kruger, M. Radajewski, I. Schneider, Microstructure and Mechanical Properties of In Situ TiB / TiC Particle-Reinforced Ti-5Al-5Mo-5V-3Cr Composites Synthesized by Spark Plasma Sintering, 49 (2018) 5671–5682.
[8] S. Zherebtsov, M. Ozerov, M. Klimova, N. Stepanov, T. Vershinina, Y. Ivanisenko, G. Salishchev, Effect of high-pressure torsion on structure and properties of Ti-15Mo/TiB metal-matrix composite, Materials (Basel). 11 (12) (2018) 2426, https://doi.org/10.3390/ma11122426.
[9] M. Bai, R. Namus, Y. Xu, D. Guan, M.W. Rainforth, B.J. Inkson, In-situ Ti-6Al-4V/TiC composites synthesized by reactive spark plasma sintering: processing, microstructure, and dry sliding wear behaviour, Wear 432-433 (2019) 202944, https://doi.org/10.1016/j.wear.2019.202944.
[10] W. Lu, X. Guo, J. Meng, F. Wang, L. Wang, D.i. Zhang, Analysis of the coupling effects of TiB whiskers and TiC particles on the fracture toughness of (TiB + TiC)/TC_4 composites: experiment and modeling, Metall. Mater. Trans. A Phys. Metall. Mater. Sci. 46 (8) (2015) 3490–3501, https://doi.org/10.1007/s11661-015-2973-6.
[11] J. Li, L. Wang, J. Qin, Y. Chen, W. Lu, D.i. Zhang, Thermal stability of in situ synthesized (TiB+La_2O_3)/Ti composite, Mater. Sci. Eng. A. 528 (15) (2011) 4883–4887, https://doi.org/10.1016/j.msea.2011.03.018.
[12] A.A.M. da Silva, J.F. dos Santos, T.R. Strohaecker, An investigation of the fracture behaviour of diffusion-bonded Ti6Al4V/TiC/10p, Compos. Sci. Technol. 66 (13) (2006) 2063–2068, https://doi.org/10.1016/j.compscitech.2005.12.018.
[13] M. Ozerov, M. Klimova, V. Sokolovsky, N. Stepanov, A. Popov, M. Boldin, S. Zherebtsov, Evolution of microstructure and mechanical properties of Ti/TiB metal-matrix composite during isothermal multiaxial forging, J. Alloys Compd. 770 (2019) 840–848, https://doi.org/10.1016/j.jallcom.2018.08.215.
[14] K. Kondoh, T. Threrujirapapong, J. Umeda, B. Fugetsu, High-temperature properties of extruded titanium composites fabricated from carbon nanotubes coated titanium powder by spark plasma sintering and hot extrusion, Compos. Sci. Technol. 72 (11) (2012) 1291–1297, https://doi.org/10.1016/j.compscitech.2012.05.002.
[15] C. Zhang, C. Guo, S. Zhang, H. Feng, J. Han, F. Kong, Y. Chen, The effect of rolling temperature on the microstructure and mechanical properties of 5 vol.% (TiBw + TiCp)/Ti composites, Jom 72 (2020) 1376–1383, https://doi.org/10.1007/s11837-019-03972-0.
[16] P. Qiu, Y. Han, G. Huang, J. Le, L. Lei, L.v. Xiao, W. Lu, Texture evolution and dynamic recrystallization behavior of hybrid-reinforced titanium matrix composites: enhanced strength and ductility, Metall. Mater. Trans. A Phys. Metall. Mater. Sci. 51 (5) (2020) 2276–2290, https://doi.org/10.1007/s11661-020-05677-5.
[17] A. Bahador, J. Umeda, H. Ghandvar, T. Asma, A. Bakar, R. Yamanoglu, A. Issariyapat, K. Kondoh, Microstructure globularization of high oxygen concentration dual-phase extruded Ti alloys via powder metallurgy route, Mater. Charact. 172 (2021), https://doi.org/10.1016/j.matchar.2020.110855 110855.
[18] A. Bahador, J. Umeda, R. Yamanoglu, T.A. Abu Bakar, K. Kondoh, Strengthening evaluation and high-temperature behavior of Ti–Fe–O–Cu–Si alloy, Mater. Sci. Eng. A. 800 (2021) 140324, https://doi.org/10.1016/j.msea.2020.140324.
[19] G. Huang, Y. Han, X. Guo, D. Qiu, L. Wang, W. Lu, D. Zhang, Effects of extrusion ratio on microstructural evolution and mechanical behavior of in situ synthesized Ti-6Al-4V composites, Mater. Sci. Eng. A. 688 (2017) 155–163, https://doi.org/10.1016/j.msea.2017.02.002.
[20] G. Huang, J. Wang, Q. Wang, Y. Lv, Y. Han, W. Lu, Microstructures and mechanical properties of hot indirect extruded in situ (TiB + TiC)/Ti6Al4V composites: Effect of extrusion temperature, Mater. Sci. Eng. A. 811 (2021), https://doi.org/10.1016/j.msea.2021.140988 140988.
[21] G. Huang, X. Guo, Y. Han, L. Wang, W. Lu, D. Zhang, Effect of extrusion dies angle on the microstructure and properties of (TiB+TiC)/Ti6Al4V in situ titanium matrix composite, Mater. Sci. Eng. A. 667 (2016) 317–325, https://doi.org/10.1016/j.msea.2016.05.021.
[22] P. Gao, H. Yang, X. Fan, S. Zhu, Unified modeling of flow softening and globularization for hot working of two-phase titanium alloy with a lamellar colony microstructure, J. Alloys Compd. 600 (2014) 78–83, https://doi.org/10.1016/j.jallcom.2014.02.110.
[23] A. Bahador, A. Issariyapat, J. Umeda, Strength e ductility balance of powder metallurgy Ti-2Fe-2W alloy extruded at high-temperature, J. Mater. Res. Technol. 14 (2021) 677–691, https://doi.org/10.1016/j.jmrt.2021.06.086.
[24] A. Bahador, J. Umeda, R. Yamanoglu, A. Amrin, A. Alhazaa, K. Kondoh, Ultrafine-grain formation and improved mechanical properties of novel extruded Ti-Fe-W alloys with complete solid solution of tungsten, J. Alloys Compd. 875 (2021) 160031, https://doi.org/10.1016/j.jallcom.2021.160031.
[25] J.L. Hutter, J. Bechhoefer, Calibration of atomic-force microscope tips, Rev. Sci. Instrum. 64 (7) (1993) 1868–1873, https://doi.org/10.1063/1.1143970.
[26] W. Wei, Q. Zhang, W. Wu, H. Cao, J. Shen, S. Fan, X. Duan, Agglomeration-free nanoscale TiC reinforced titanium matrix composites achieved by in-situ laser additive manufacturing, Scr. Mater. 187 (2020) 310–316, https://doi.org/10.1016/j.scriptamat.2020.06.057.
[27] A. Issariyapat, P. Visuttipitukul, T. Song, A. Bahador, J. Umeda, M.a. Qian, K. Kondoh, Tensile properties improvement by homogenized nitrogen solid solution strengthening of commercially pure titanium through powder metallurgy process, Mater. Charact. 170 (2020) 110700, https://doi.org/10.1016/j.matchar.2020.110700.
[28] J. Umeda, T. Tanaka, T. Teramae, S. Kariya, J. Fujita, H. Nishikawa, Y. Shibutani, J. Shen, K. Kondoh, Microstructures analysis and quantitative strengthening evaluation of powder metallurgy Ti–Fe binary extruded alloys with (α+β)-dual-phase, Mater. Sci. Eng. A. 803 (2021) 140708, https://doi.org/10.1016/j.msea.2020.140708.
[29] L. Germain, N. Gey, M. Humbert, P. Vo, M. Jahazi, P. Bocher, Texture heterogeneities induced by subtransus processing of near α titanium alloys, Acta Mater. 56 (16) (2008) 4298–4308, https://doi.org/10.1016/j.actamat.2008.04.065.
[30] Q. Yan, B. Chen, N. Kang, X. Lin, S. Lv, K. Kondoh, S. Li, J.S. Li, Comparison study on microstructure and mechanical properties of Ti-6Al-4V alloys fabricated by powder-based selective-laser-melting and sintering methods, Mater. Charact. 164 (2020) 110358, https://doi.org/10.1016/j.matchar.2020.110358.
[31] M. Frary, S. Abkowitz, S.M. Abkowitz, D.C. Dunand, Microstructure and mechanical properties of Ti/W and Ti-6A1-4V/W composites fabricated by powder-metallurgy, Mater. Sci. Eng. A. 344 (2003) 103–112, https://doi.org/10.1016/S0921-5093(02)00426-4.
[32] D. Yadav, R. Bauri, Processing, microstructure and mechanical properties of nickel particles embedded aluminium matrix composite, Mater. Sci. Eng. A. 528 (3) (2011) 1326–1333, https://doi.org/10.1016/j.msea.2010.10.035.
[33] Z. Liu, P. Li, L. Xiong, T. Liu, L. He, High-temperature tensile deformation behavior and microstructure evolution of Ti55 titanium alloy, Mater. Sci. Eng. A. 680 (2017) 259–269, https://doi.org/10.1016/j.msea.2016.10.095.
[34] D.E. Kramer, M.F. Savage, L.E. Levine, AFM observations of slip band development in Al single crystals, Acta Mater. 53 (17) (2005) 4655–4664, https://doi.org/10.1016/j.actamat.2005.06.019.
[35] E. Soppa, P. Doumalin, P. Binkele, T. Wiesendanger, M. Bornert, S. Schmauder, Experimental and numerical characterisation of in-plane deformation in two-phase materials, Comput. Mater. Sci. 21 (3) (2001) 261–275, https://doi.org/10.1016/S0927-0256(01)00170-7.
[36] Y. Tanaka, J.-M. Yang, Y.F. Liu, Y. Kagawa, Characterization of nanoscale deformation in a discontinuously reinforced titanium composite using AFM and nanolithography, Scr. Mater. 56 (3) (2007) 209–212, https://doi.org/10.1016/j.scriptamat.2006.10.015.
[37] M.G. Elkhateeb, Y.C. Shin, Molecular dynamics-based cohesive zone representation of Ti6Al4V/TiC composite interface, Mater. Des. 155 (2018) 161–169, https://doi.org/10.1016/j.matdes.2018.05.054.
[38] P. Wanjara, R.A.L. Drew, J. Root, S. Yue, Evidence for stable stoichiometric Ti2C at the interface in TiC particulate reinforced Ti alloy composites, Acta Mater. 48 (7) (2000) 1443–1450, https://doi.org/10.1016/S1359-6454(99)00453-X.
[39] Y. Hao, J. Liu, J. Li, S. Li, Q. Zou, X. Chen, Rapid preparation of TiC reinforced Ti6Al4V based composites by carburizing method through spark plasma sintering technique, Mater. Des. 65 (2015) 94–97, https://doi.org/10.1016/j.matdes.2014.09.008.
[40] J. Wang, L. Li, C. Tan, H. Liu, P. Lin, Microstructure and tensile properties of TiCp/Ti6Al4V titanium matrix composites manufactured by laser melting

deposition, J. Mater. Process. Technol. 252 (2018) 524–536, https://doi.org/10.1016/j.jmatprotec.2017.10.005.
[41] D.G. Konitzer, M.H. Loretto, Microstructural assessment of Ti6Al4V-TiC metal-matrix composite, Acta Metall. 37 (1989) 397–406, https://doi.org/10.1016/0001-6160(89)90224-1.
[42] L. Zheng, F. Li, Y. Zhou, R. Koc, Preparation, microstructure, and mechanical properties of TiB_2 using Ti_3AlC_2 as a sintering aid, J. Am. Ceram. Soc. 95 (6) (2012) 2028–2034, https://doi.org/10.1111/j.1551-2916.2012.05204.x.
[43] Y. Wang, J. Feng, Z. Chen, X. Song, J. Cao, Wetting of microstructured alumina fabricated by epitaxial growth of $Al_4B_2O_9$ whiskers, Appl. Surf. Sci. 357 (2015) 766–770, https://doi.org/10.1016/j.apsusc.2015.09.097.
[44] G. Ma, C. Yu, B. Tang, Y. Li, F. Niu, D. Wu, G. Bi, S. Liu, High-mass-proportion TiCp/Ti_6Al_4V titanium matrix composites prepared by directed energy deposition, Addit. Manuf. 35 (2020) 101323, https://doi.org/10.1016/j.addma.2020.101323.
[45] S. Luo, T. Song, B. Liu, J. Tian, M.a. Qian, Recent advances in the design and fabrication of strong and ductile (tensile) titanium metal matrix composites, Adv. Eng. Mater. 21 (7) (2019) 1801331, https://doi.org/10.1002/adem.v21.710.1002/adem.201801331.
[46] A. Bahador, J. Umeda, R. Yamanoglu, H. Ghandvar, A. Issariyapat, T.A. Abu Bakar, K. Kondoh, Deformation mechanism and enhanced properties of Cu-TiB_2 composites evaluated by the in-situ tensile test and microstructure characterization, J. Alloys Compd. 847 (2020) 156555, https://doi.org/10.1016/j.jallcom.2020.156555.
[47] J. Shen, B. Chen, J. Umeda, K. Kondoh, Advanced mechanical properties of a powder metallurgy Ti-Al-N alloy doped with ultrahigh nitrogen concentration, Jom 70 (5) (2018) 626–631, https://doi.org/10.1007/s11837-018-2780-9.
[48] Y. Guo, T.B. Britton, A.J. Wilkinson, Slip band-grain boundary interactions in commercial-purity titanium, Acta Mater. 76 (2014) 1–12, https://doi.org/10.1016/j.actamat.2014.05.015.
[49] R.L. Fleischer, Substitutional solution hardening, Acta Metall. 11 (3) (1963) 203–209, https://doi.org/10.1016/0001-6160(63)90213-X.